Experimental Evaluation of the Aerodynamic Performance of a Large-Scale High-Lift Morphing Wing

Franco Auteri[a,1,*], Alberto Savino[a,2], Alex Zanotti[a,3], Giuseppe Gibertini[a,1], Daniele Zagaglia[a,4], Yannick Bmegaptche Tekap[b,2], Marianna Braza[b,5]

[a] *Dipartimento di Scienze e Tecnologie Aerospaziali, Politecnico di Milano, Milan, Italy*
[b] *Institut de Mécanique des Fluides de Toulouse, Toulouse, France*

Abstract

The Smart Morphing & Sensing (SMS) project was a multi-disciplinary upstream project that investigated the use of intelligent electro-active actuators to modify the lifting surface of an aircraft. In particular, the attention of the project was focused on trailing-edge, high-lift morphing devices aimed to obtain the optimal shapes to improve the aerodynamic performance of the wing of a large passenger aircraft. The present work describes the experimental assessment of the morphed aerodynamic shapes of the high-lift morphing flap developed during the project. Wind-tunnel tests were performed using a large-scale wing prototype reproducing a section of a full-scale wing of a large passenger aircraft. Several quantities were measured during the tests. Pressure measurements performed in the mid-span section of the wing showed

*Corresponding author
Email addresses: franco.auteri@polimi.it (Franco Auteri), alberto.savino@polimi.it (Alberto Savino), alex.zanotti@polimi.it (Alex Zanotti), giuseppe.gibertini@polimi.it (Giuseppe Gibertini), daniele.zagaglia@polimi.it (Daniele Zagaglia), yannick.bmegaptchetekap@imft.fr (Yannick Bmegaptche Tekap), marianna.braza@imft.fr (Marianna Braza)
[1]Associate Professor
[2]PhD Student
[3]Assistant Professor
[4]Research Associate
[5]Director of Research CNRS, IMFT

an increase of the lift provided by the cambered morphed shape of the flap in take-off configuration and an increase of both the lift coefficient and the wing efficiency in landing configuration. Particle Image Velocimetry surveys enabled us to obtain an insight in the flow physics behind the measured performance of the morphing flap. Moreover, the deformation of the morphing flap was measured by optical systems to check the actual shape. The current study shows the potential of morphed trailing-edge flap configurations to increase aerodynamic performance for large-scale fixed-wing aircraft.
Keywords: Morphing, Wind Tunnel, Aerodynamics, High-Lift Wing

Nomenclature

1. INTRODUCTION

With the aim to reduce the operational costs of aircraft and the environmental impact of the aviation industry, particular effort is being devoted to study efficient systems that can limit energy consumption and noise [**?**]. A possible way to fulfill this goal is to improve the aerodynamic performance of aircraft. The mission of an aircraft is composed by several flight conditions, each one requiring a different shape of the wing to reach an adequate aerodynamic performance. This change of shape is obtained, in current commercial aircraft, deploying high-lift devices. The ability to deform the main airfoil and the flaps during a mission has the potential to produce a non-negligible fuel saving [**?**]. This kind of deformations are called *morphing* [**?**]. The concept of morphing applied to the improvement of aircraft-wing performance has been widely developed in literature. An overview of different morphing concepts for aircraft is provided by Barbarino et al. [**?**]. In particular, an efficient way to improve airliner aerodynamic performance is to control the camber of the trailing-edge region of the wing. The work by Lyu et al. [**?**]

showed that morphing a limited part of the airfoil chord could produce the same effectiveness with respect to entirely morphed airfoils.

In the recent years, several European research programs, such as Clean-Sky (`http://cleansky.eu/`) and SARISTU [**?**], focus their attention on the reduction of operating cost for aircraft as well as on improving the aerodynamic performance. In particular, SARISTU was focused on adaptive morphing trailing edge actuated by servomotors and hinges that allow for camber control during the different flight conditions of the aircraft.

In the Horizon 2020 (H2020) framework, the Smart Morphing & Sensing (SMS) project N° 723402 (`http://smartwing.org/SMS/EU/`) has been a multi-disciplinary upstream project that employed intelligent electro-active actuators to modify the lifting structure of an aircraft to obtain the optimal shape with respect to the aerodynamic performance (high lift and low drag). The approach pursued in this project led to an electro-active hybrid morphing concept, inspired from the flight of large-span hunting birds [**?**]. This concept is based on the implementation of efficient systems to operate at different time and length scales, i.e. a low frequency (< 1 Hz) camber control that could lead to about 10% of the chord deformation at trailing edge and a higher frequency vibrating trailing edge that could be deformed by fractions of millimeters up to 400 Hz. With this aim, two classes of smart electro-active materials (smart actuators) were employed in the design of a morphing prototype of the Airbus A320 flap. Shape Memory Alloys (SMA) were used for the high deformations and piezo-actuators of Macro-Fiber Composite type (MFC) ensuring the higher-frequency vibrations were used to operate at small amplitudes [**?**]. A reduced scale (RS) prototype of the A320 wing was manufactured and tested in the wind tunnel [**?**]. The experimental tests showed that electro-active morphing can provide an

enhanced aerodynamic performance in terms of lift increase and drag reduction and can reduce the amplitude of the instability modes associated to aerodynamic noise. Moreover, in the framework of the same project, a large-scale (LS) prototype of the morphing flap of the A320 wing, based on electro-mechanical actuators (EMAs) and SMAs, was designed and manufactured at SMS Coordinator's Laboratory (Institut de Mécanique des Fluides de Toulouse) in collaboration with the LAPLACE Laboratory (Laboratoire Plasma et Conversion d'Energie, Toulouse), enabling high camber morphing capable to sustain and transmit the aerodynamic forces in full-scale conditions. A detailed description of the design of this LS prototype is provided in [**?** **?**].

The present work describes the experimental evaluation of the performance of the LS morphing flap on an almost full-scale wing prototype. The wing section is representative of the external flap region of the main wing of a large passenger aircraft of the class of the Airbus A320, and the scaling factor is in the range 75%-80%. The main goal of the wind-tunnel tests was to measure the aerodynamic loads acting on the wing to evaluate the effectiveness of the different morphed shapes that could be provided by the trailing-edge flap to improve the aerodynamic performance of the wing section. In particular, the main parameters used to assess the effectiveness of the morphed shapes were the wing lift and aerodynamic efficiency produced in landing condition as well as the aerodynamic efficiency in take-off. With this aim, a comprehensive test campaign including different measurement techniques was performed in the large wind tunnel of Politecnico di Milano (GVPM). Thanks to the large size of the test section allowing the installation of an almost full-scale wing section of a large passenger aircraft wing and by virtue of the quite high velocity that can be reached in the wind tunnel, the tests

could be performed at high Reynolds numbers, thus providing indications of the performance of the flap in full-scale aircraft applications, particularly for take-off and landing maneuvers.

The aim was to show the relatively high sensitivity of wing performance with respect to optimal flap shapes previously studied by numerical simulation by IMFT in the SMS framework and, consequently, the potential of the morphing approach for flapped-wing optimisation. Moreover, the comprehensive experimental database represents an interesting benchmark for the validation of CFD simulations to be used to extend the study of the flap performance to real-flight conditions of the full aircraft.

The wind-tunnel test activity described in the present work is quite unusual, particularly for research projects. Usually, scaled models are tested in the wind tunnel [**?**]. Indeed, due to the large size of the wing model (span of 4 m, airfoil chord of 2.4 m and flap chord of 1 m, leading to a total chord in take-off configuration of 2.7 m), a limited number of wind-tunnel facilities are suitable to test a wing section of a large-passenger aircraft almost at full scale, and this requires a relevant investment. Consequently, very few similar works are described in the scientific literature. One of them, by Dobrzinsky et al. [**?**], describs wind-tunnel experiments on a full scale high-lift wing of a Airbus A320 dedicated to airframe noise reduction. Therefore, in the present work particular attention is dedicated to the description of the wind-tunnel test design as one of its goals is to identify and disseminate the set-up and execution of complex experimental activities involving the use of large-scale wing models. In particular, due to the large size of the model with respect to the size of the test section, a check of the compatibility of the model with the quality of the fluid vein was performed in a preliminary experiment using a scaled model of the wind tunnel. Moreover, particular care was dedicated

to the sizing and geometrical modelling of the wing section, including static and dynamic structural verification since very high loads were expected. The wind-tunnel campaign included pressure measurements on the mid-span section of the model to evaluate the aerodynamic performance of different morphed shapes provided by the flap for both take-off and landing configurations. Moreover, Particle Image Velocimetry surveys were performed over the upper surface region of the trailing edge of the flap to obtain a detailed insight in the flow physics involved in the morphing-flap functioning. An evaluation of the model deformation due to the aerodynamic loads is also performed during the wind-tunnel tests by means of optical measurements of the flap shape.

This paper is organized as follows. The experimental set-up, including the large-scale model design and the measurement system used in the wind-tunnel campaign, is described in Sec. §2. The main results of the wind-tunnel campaign are reported and discussed in Sec. §3. Conclusions about the effectiveness of morphing the trailing-edge flap in different flight configurations are reported in Sec. §4.

2. EXPERIMENTAL SET-UP

The present section describes the experimental set-up used for the wind tunnel campaign of the large-scale wing model equipped with the trailing-edge morphing flap. The test activity was performed in the large wind tunnel of Politecnico di Milano (GVPM). The GVPM is a closed-circuit wind tunnel, arranged in a vertical layout with two test sections located on the opposite sides of the loop, as can be observed in Fig.1(a). The present tests were performed in the 4 m wide x 3.84 m high Low-Turbulence Test Section [**?**] (see the particular in Fig. 1(b)), characterised by a maximum wind speed of

55 m/s and a turbulence level less than 0.1%.

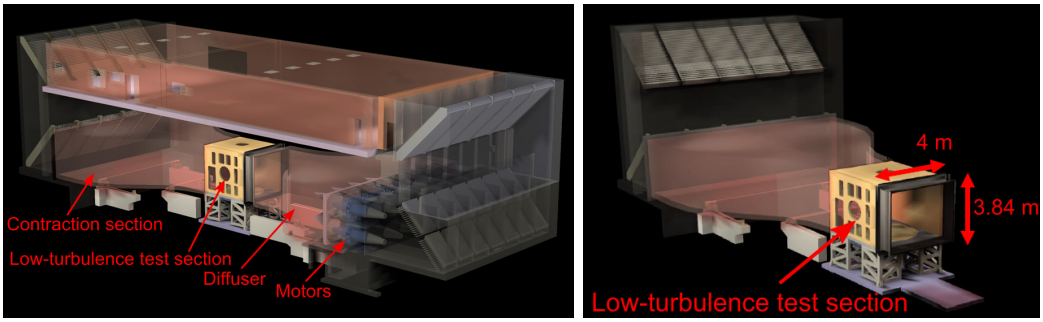

(a) (b)

Figure 1: The wind tunnel of Politecnico di Milano (GVPM): (a) general layout of GVPM; (b) particular of the Low-Turbulence Test Section.

2.1. Design of the large-scale wing model

The wind-tunnel model was designed to reproduce an almost full-scale wing section of a large passengers aircraft, like the Airbus A320, equipped with the prototype of the morphing flap designed in the framework of the SMS project [**?** **?**]. The wing model spanned the whole 4 m width of the test section and had a chord or 2.4 m. The morphing flap span was 2 m with a chord of 1 m. A framed structure has been selected for the wing model, with a structural skeleton and a non-loaded skin (see Fig. 2(a)). The skeleton is composed of two steel spars that extend along the full span of the model and ten aluminium ribs transferring the aerodynamic loads from the skin to the spars. Two force ribs, among the ten, are used to sustain the flap and to transfer its loads to the spars. The external skin is composed by 1.5 mm thick aluminium-alloy panels in the low-curvature regions and molded fiberglass-reinforced-composite panels for the high-curvature regions, namely the leading edge and the trailing edge in the bay hosting the flap (see Fig.2(b)). For a detailed description of the morphing-flap model, the reader is directed to [**?** **?**]

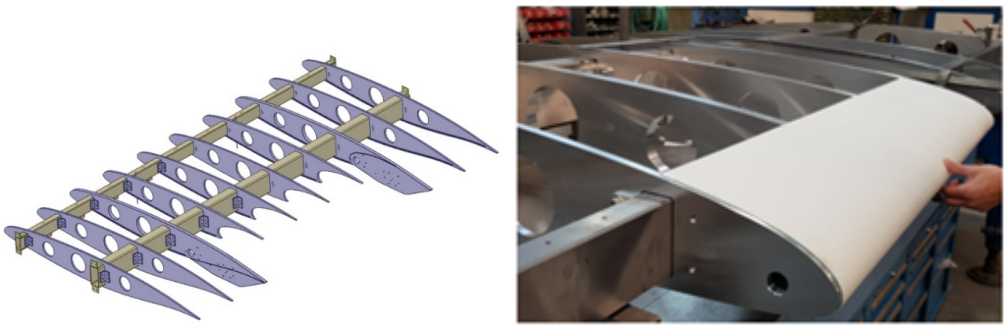

(a) (b)

Figure 2: Layout of the large-scale wing model: (a) CAD model of the wing skeleton, (b) particular of the fiberglass-reinforced composite panels used on the external skin at the leading edge.

The morphing flap was fastened to the wing structure by a mechanical interface allowing the positioning of the flap in take-off and landing configuration. The model was installed in the wind-tunnel test section by fixing the two spars to the walls. In particular, the spar at mid-chord was connected to the wind-tunnel walls through two spherical roller bearings that allowed the change of the angle of attack of the wing and the accommodation of small misalignment between the shafts. Figure 3 shows two views of the wing model equipped with the morphing flap installed in the GVPM test section.

The design phase of the wing model included static and dynamic structural checks to verify that the safety and stiffness requirements were satisfied before wind-tunnel tests. The static structural checks were carried out using finite-element analysis and the aerodynamic loads computed through CFD in landing condition, where the highest loads of the test envelope were expected. With reference to the main results of the calculated structural dynamic response, the first bending mode was obtained at 35 Hz, while the first torsional mode was obtained at a frequency over 145 Hz, thus ensuring ample margins to avoid flexion-torsional couplings. In this design phase the flap was

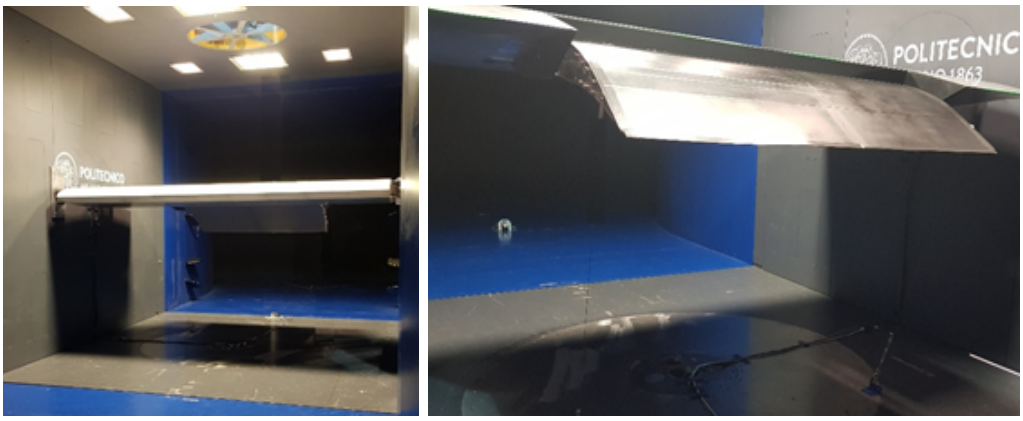

(a) (b)

Figure 3: The wing model installed in the GVPM test section.

modelled as a rigid body using the mass and inertia properties of the real flap.

Moreover, given the considerable size of the model, especially with respect to the wind tunnel, a preliminary test was performed to verify if the high flow deflection induced by such a large model could cause the stall of the diffuser. The test was performed using the 1:9 scaled model of the GVPM that was built and used in the past years to test the design choices that led to the construction of the full-scale wind tunnel [**?**]. A scaled model of the wing and flap was manufactured by rapid prototyping to be installed in the test section of the scaled wind tunnel. In particular, the compatibility test was performed with the wing model reproducing the landing configuration at the highest angle of attack planned for the wind-tunnel tests, i.e. $\alpha = 8°$. This configuration was selected for the compatibility tests as it represents the configuration providing the highest deflection of the flow and wind-tunnel blockage. Micro-tufts attached to the internal surface of the wind-tunnel scaled model showed no massive separation in the diffuser. Moreover, the high blockage provided by this wing-model configuration provided a 20%

reduction of the maximum achievable free-stream velocity of the wind tunnel. Consequently, the wind-tunnel tests in the GVPM of the large-scale wing model were performed with a maximum free-stream velocity of 40 m/s.

2.2. Design of the morphing flap

The trailing-edge morphing flap has been designed starting from a baseline shape provided by Airbus, based on A320 commercial aircraft. The flap has 1 m chord and 2 m span. The internal structure of the morphing flap is based on 14 aluminium articulated ribs, connected by one aluminium main spar, where actuators control the rotations of the elements around four hinges (Figure 4). The articulated ribs define the geometry and carry the other components. They have to withstand the internal and external (i.e. aerodynamic) forces, while being low weight. Hinges allow the rotation of the articulated ribs. Steel-TEFLON gliding bearings have been selected for the hinges since they are suitable for low rotation velocities and they are compact, lightweight and generate low frictional torque. The actuators are responsible for the shape control and have to counteract aerodynamic forces, mainly. They are composed of SMA wires or EMA actuators. The skin guarantees the air tightness of the wing, transmits the aerodynamic forces to the structure and ensures a smooth morphed shape. In particular, as only static wing morphed shapes were tested in the present study, adhesive tape was used to restore the smoothness of the surface in each morphing configuration. The skin must endure deformation without unexpected displacements like bumps or wrinkles. Mechanical stops are provided to limit the rotations of the articulations, thus preventing overloads in actuators.

The structure has been verified with static loads. A chord-wise loading has been specified based on potential flow simulations, equivalent to 1.5 tons of aerodynamic upward forces. The calculated load has been distributed on

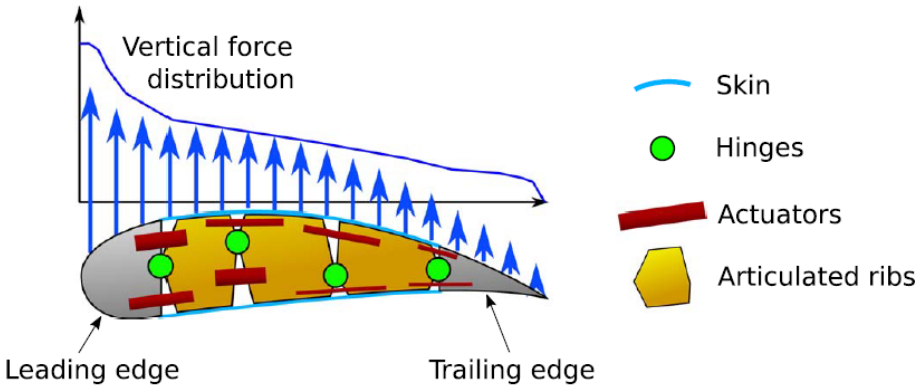

Figure 4: Flap concept, equipped with SMA actuators.

the structure by applying 70% on the upper surface and 30% on the lower surface, see Figure 5. The flap main solicitations come from span-wise bending moment and torsion. The articulation axes are span-wise, therefore the span-wise bending stiffness is not compromised. Regarding the torsional stiffness, the flap is cut in multiple wing-boxes linked together by the actuators and the hinges. All the torsion forces are transmitted through the actuators. An eigenvalue analysis has also been carried out to check that the lowest natural frequencies were sufficiently separated from each other. The modal analysis showed the absence of local modes, i.e. all modes involve all the components of the structure. The first mode, detected at a frequency of around 48 Hz, is related to the morphing deformation. The second mode is above 100 Hz and therefore, the modal density which represents the number of resonant modes of the structure in a frequency band is relatively low. This represented an indicator of the design quality, because many instabilities, like flutter, arise from the coupling between two or more modes.

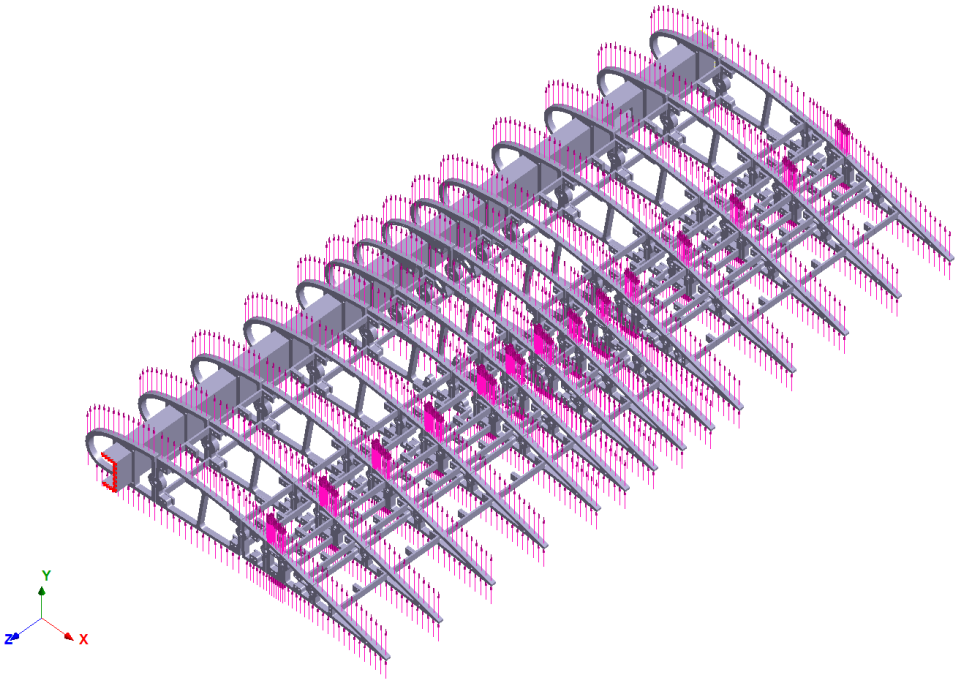

Figure 5: Flap internal structure and design loads.

2.3. Measurement set-up

The wind-tunnel campaign took advantage of different measurement techniques. In particular, the aerodynamic performance of the wing equipped with the morphing flap was evaluated by means of pressure measurements performed on the mid-span section of the model. This approach was selected because a direct measurement of the very high aerodynamic loads expected for these tests by means of the strain gauge balances available at GVPM was considered unfeasible due to the large dimensions of the model and the high speed. Additionally, two-dimensional PIV surveys were performed over the upper surface region of the flap for some selected wing configurations. Finally, non-intrusive optical measurements were used to evaluate the deformation of the flap during the wind-tunnel tests.

2.3.1. Set-up of the pressure measurements

The wing model surface was equipped with a total of 141 static pressure taps as illustrated in Fig. 6.

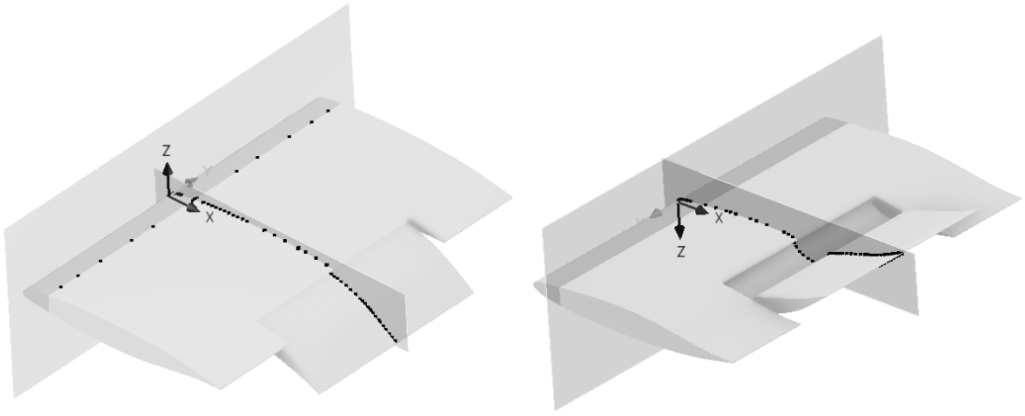

Figure 6: Layout of the pressure-tap distribution on the suction side (left) and pressure side (right) of the model surface

The pressure taps were mainly located on the symmetry plane of the wing model, including the flap. In order to evaluate the flow symmetry and any potential three-dimensional flow effects, additional static pressure taps were placed span-wise on the suction side of the main wing close to the leading edge region. A further set of chord-wise taps were installed along two sections at ±5 cm on either side of the symmetry plane. The pressure measurements were performed by means of five 32 ports Pressure Systems Inc. pressure scanners embedded inside the model with different full-scale values (all providing an accuracy of 0.1% F.S.). In particular, three scanners with 1 PSI F.S. were connected to the taps in trailing-edge region, while one scanner with 2.5 PSI F.S. and another one scanner with 10 PSI F.S. were connected to the pressure taps positioned upstream, towards the leading edge to provide a higher full-scale where the highest peaks of pressure are expected due to the high-lift configurations to be tested. The average

pressure distribution was obtained over an acquisition time of 20 seconds.

2.3.2. PIV set-up

Two-dimensional PIV surveys were performed over the suction side of the trailing edge of the flap. The aim of these measurements was to characterise the flow behaviour in this region which is particularly critical from the viewpoint of performance. Indeed, in order to investigate in detail the role of the flow physics on the performance of the morphing flap in landing and take-off configuration, particular attention was payed to survey possible regions of flow separation for the different shapes of the flap. Moreover, the flow fields evaluated by this measurement technique enabled us to produce an experimental database to be used to validate CFD simulations. The PIV system was configured to measure the in-plane velocity components on the longitudinal X–Z symmetry plane in order to avoid the regions where three-dimensional effects are not negligible due to the wind-tunnel walls. The area of investigation covered almost half of the suction side of the morphing flap and a small region of the wake past the flap trailing edge. This area was surveyed by means of two adjacent windows with a small overlapping between them. The dimension of each measurement window was 345 mm $\times$ 110 mm. The position of the measurement windows with respect to the flap is illustrated in Fig. 7.

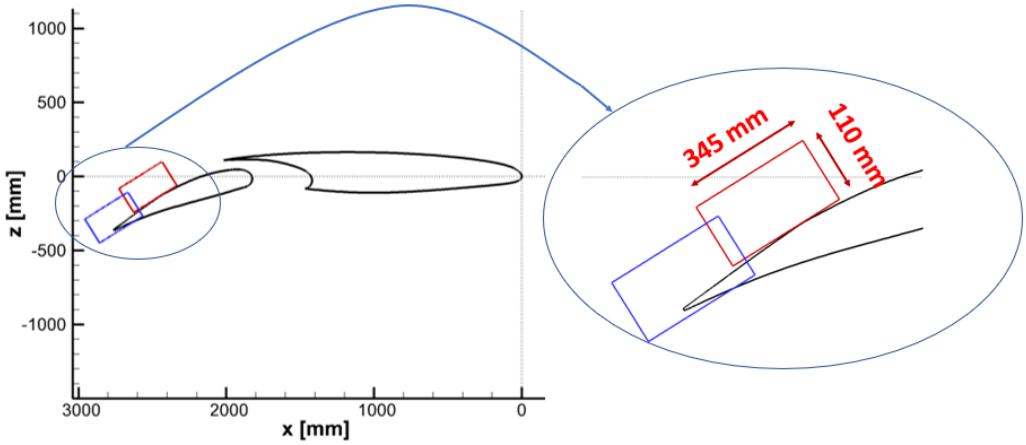

Figure 7: PIV measurement windows on the longitudinal x-z symmetry plane of the wing model. Position and size of the measurement windows with respect to the flap.

The PIV system consisted of a Litron NANO-L-200-15 Nd:Yag double pulsed laser with 200 mJ output energy and a wavelength of 532 nm, and two Imperx ICL-B1921M CCD cameras with a 12 bit, 1952 $\times$ 1112 pixel array. The layout of the PIV instrumentation is illustrated in Fig. 8. The laser was mounted on the roof of the wind-tunnel test section and the light sheet passed through an acrylic-glass window as shown in Fig. 8. The cameras were arranged in tandem configuration to provide the simultaneous acquisition of the two adjacent windows for each test configuration. In particular, the cameras were mounted on two sliding aluminium profiles attached to the side wall of the test section to move the image planes along two orthogonal directions (see the particular in Fig. 8). This solution enabled us to move the measurement windows following the displacement of the flap when the configuration or the angle of attack were changed.

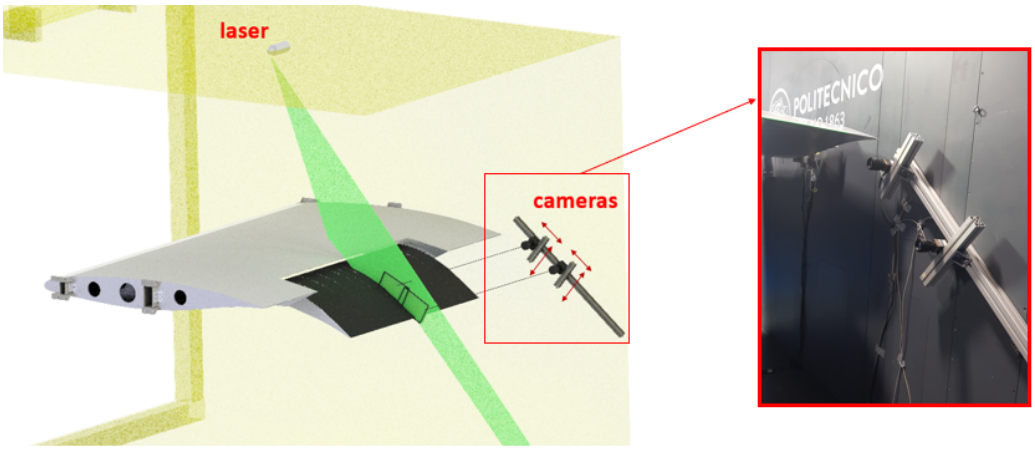

Figure 8: Layout of the PIV instrumentation in the GVPM wind-tunnel test section.

Each camera was equipped with a Nikkor 50 mm lens. The synchronisation of the two laser pulses with the image-pair exposure was controlled by a 6-channel Quantum Composer QC9618 pulse generator. A particle generator with Laskin atomiser nozzles was used to seed the entire test-section. The particles consisted of small oil droplets with a diameter in the range of 1–2 μm. The image-pair analysis was performed using PIVview, a software developed by PIVTEC in close cooperation with the PIV groups of the German Aerospace Center (DLR) in Gottingen and Koln [**?**]. The correlation of the image pairs was performed considering an interrogation window of 64 x 64 pixels with an overlap of 50%. This leads to a resolution of one measurement point every 5.7 mm. All the resulting velocity fields presented in this work were averaged over 500 image pairs. The accuracy of the PIV measurement can be estimated considering a maximum displacement error of 0.1 px, as found in [**?**], that corresponds to a maximum error less than 1% of the maximum free-stream velocity.

2.3.3. Shape-measurement set-up

The ultimate performance of a morphing flap can be influenced by its deformation due to the intrinsic flexibility of the structure. Therefore, the deformation produced by the aerodynamic loading was measured to ensure that the performance was not biased by an excessive deformation of the flap and to provide a quantitative indication of the real shape of the morphed flap for a future robust comparison with CFD simulation results. The displacement and deformation of the flap produced by the aerodynamic loading were measured exploiting an optical non-intrusive technique [**?**]. The technology here employed, that is typically used for motion capture, exploited 8 Qualisys Miqus M3 cameras providing a resolution of 1824 $\times$ 1088 pixels, with an acquisition frequency of 100 Hz. The cameras were mounted on the walls of the test section as shown in Fig. 9.

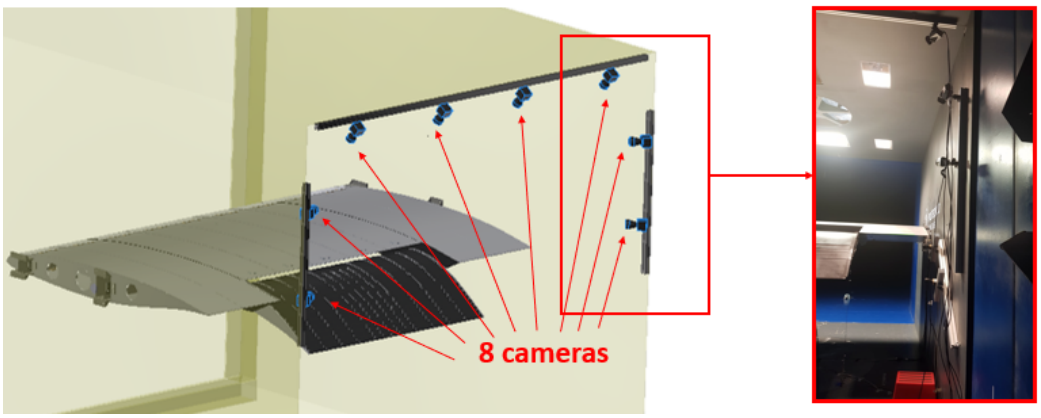

Figure 9: Set-up of the cameras in the GVPM test section for the measurement of the morphing-flap deformation.

Since this technology suffers from the reflection of infrared wavelengths, the entire flap and the force ribs were painted in matt black. The flap suction side was equipped with a marker system that consisted of 21 adhesive-tape targets reflecting infrared wavelengths that were positioned along the

span-wise and chord-wise directions, as can be observed in Fig. 10. A reference system made of 4 spherical markers placed on a single bracket was also placed on the model to refer the displacement of the markers on the flap to the main wing. All the images capturing the marker positions from several points of views were processed using Qualisys Track Manager software [**?**] to reconstruct the relative displacements of the morphing-flap surface [**?**]. We compared the standard deviation of the wind-on measurements with that with no wind to assure that camera vibrations did not contaminate the displacements.

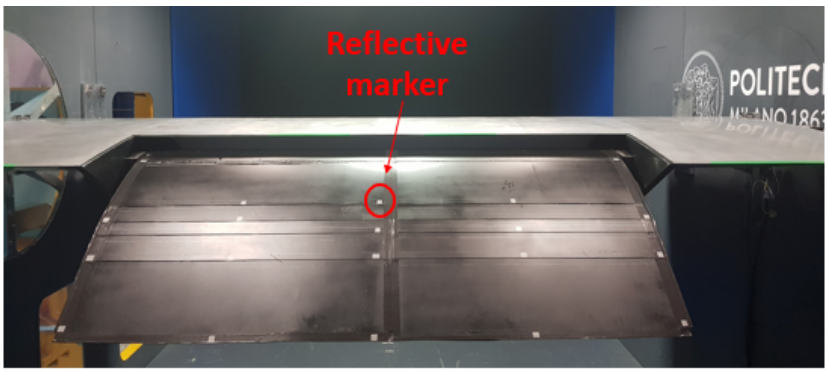

Figure 10: Layout of the adhesive reflective markers on the morphing flap

The system generated an output composed of the measurements of the displacements of each marker with respect to the three directions of a fixed reference system. From these measurements, a surface grid was built through linear interpolation to evaluate the displacement of the flap surface in wind-on conditions with respect to the unloaded condition at zero free-stream velocity. Figure 11 shows the interpolated grid built from the marker data, where also the position of the reference fixed triad made by 4 spherical markers on the main wing is visible.

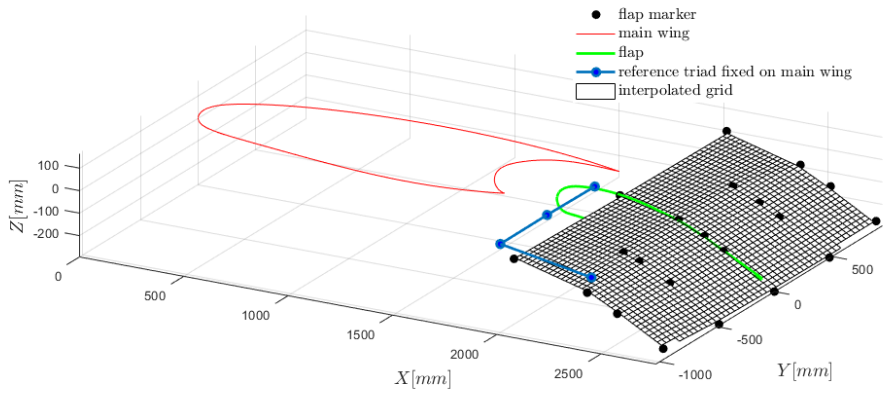

Figure 11: Position of the markers for measuring the displacement and interpolated grid for the take-off configuration of the flap, baseline geometry.

3. RESULTS

The wind tunnel campaign focused on the investigation of the effects of different morphing-flap shapes on the performance of the wing in take-off and landing conditions. In particular, three different shapes of the morphing flap characterised by different cambers were tested for each flight condition, as shown in Fig. 12.

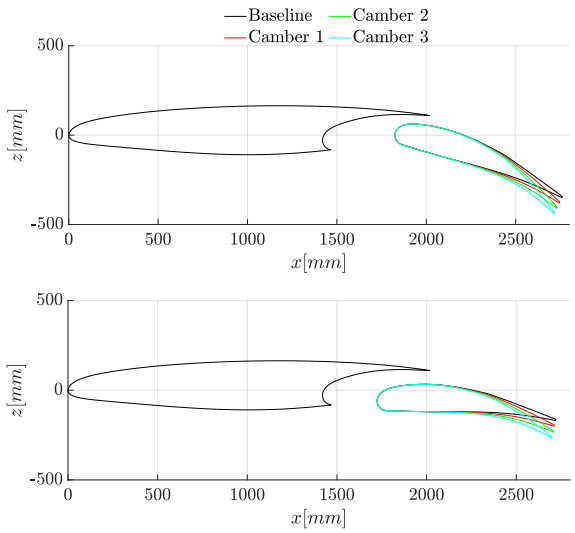

Figure 12: Flap cambering configurations tested for take-off (bottom) and landing (top) conditions.

The tests were performed sweeping the angle of attack of the wing model in the range between $\alpha = 0°$ and $\alpha = 8°$ with a step of 2°. Since preliminary CFD simulations of the wind-tunnel test set-up at $\alpha = 8°$ showed massive separation on the whole wing and this condition was considered not interesting for the project, the tests in landing configuration were not performed at this angle of attack. The tests were repeated for three values of the free-stream velocity V_∞, i.e. 30 m/s, 34.1 m/s and 40 m/s, to evaluate effects of the Reynolds number and of the flap deformation on the wing performance. The Reynolds numbers corresponding to the three tested speeds were $4.8{\times}10^6$, 5.5×10^6 and 6.4×10^6, respectively. Pressure measurements were performed for all the configurations tested. PIV surveys and shape measurements were performed for a selected set of test configurations based on the results of aerodynamic performance measurements.

Fig. 13 shows the pressure distribution measured on the entire set of pressure taps for the most critical test condition performed during the wind

tunnel campaign, i.e. the landing configuration at the highest angle of attack ($\alpha = 6°$) with the morphing flap configured with highest camber. Very good symmetry and two-dimensionality of the flow from the pressure distribution can be observed from the available measurement over the wing model.

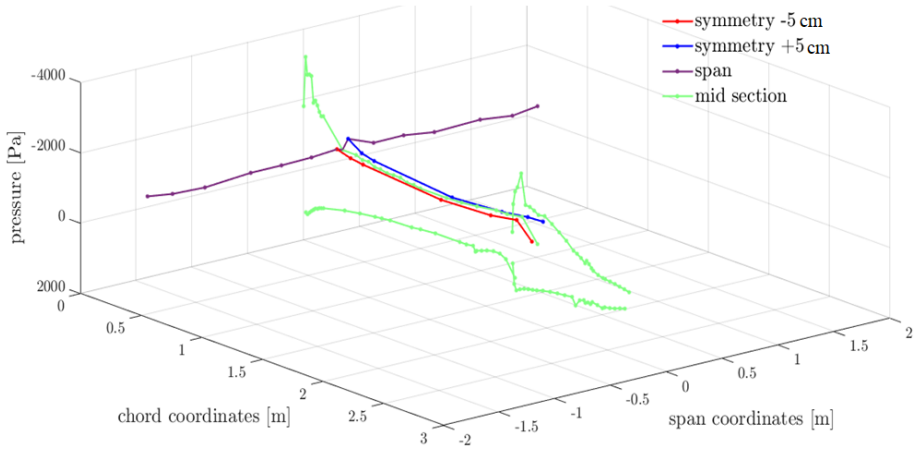

Figure 13: Pressure measured on all the model pressure taps for the landing configuration and morphing flap with Camber 3, $\alpha = 6°$, $V_\infty = 40$ m/s.

3.1. Aerodynamic-performance measurements

Figure 14 shows the lift coefficient C_L evaluated by integrating pressure measurements over the mid-span section of the wing as a function of the angle of attack for both take-off and landing configurations for the three free-stream velocities investigated in this campaign. In particular, for the take-off configuration, Fig. 14(a) shows that the Camber 1 shape of the morphing flap provides a negligible increase of lift over the entire range of angles of attack tested. In contrast, a remarkable lift increase is observed for Camber 2 and Camber 3. Moreover, it can be noticed that the lift coefficient for the take-off configuration is marginally affected by the magnitude of the wind speed. Indeed, increasing the free-stream velocity, the C_L slightly decreases. Thus, the effects of the Reynolds number and of the flap deformation are negligible

for the lift coefficient in this configuration. The histogram in Fig. 15(a), showing the percentage variation of lift with respect to baseline configuration for the mid free-stream velocity tested, highlights quantitatively the increase of C_L provided by the different cambered shapes of the morphing flap. A remarkable increase of the C_L is observed in particular for Camber 2 and Camber 3. The lift variation is higher increasing the camber of the morphing flap shape and decreases as the angle of attack is increased. Indeed, Camber 3 provides more than 20% increase of lift at zero angle of attack while an increase of about 7% of lift coefficient is measured at the highest incidence.

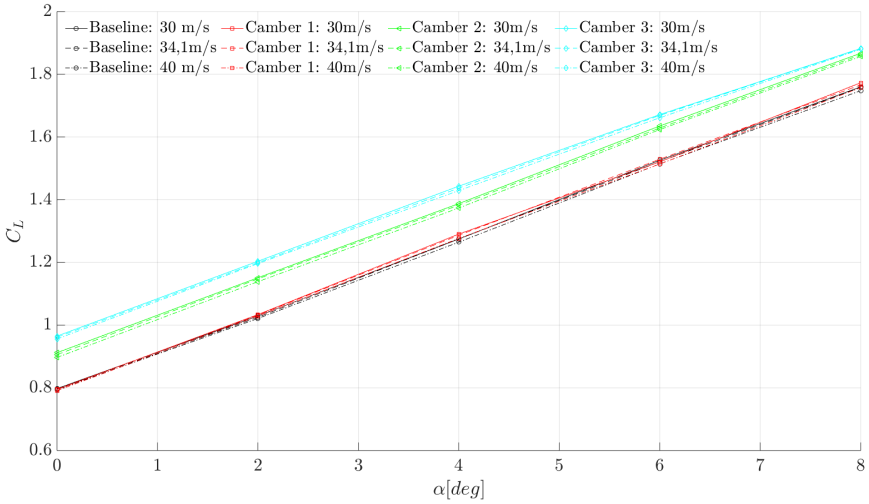

(a) Take-off

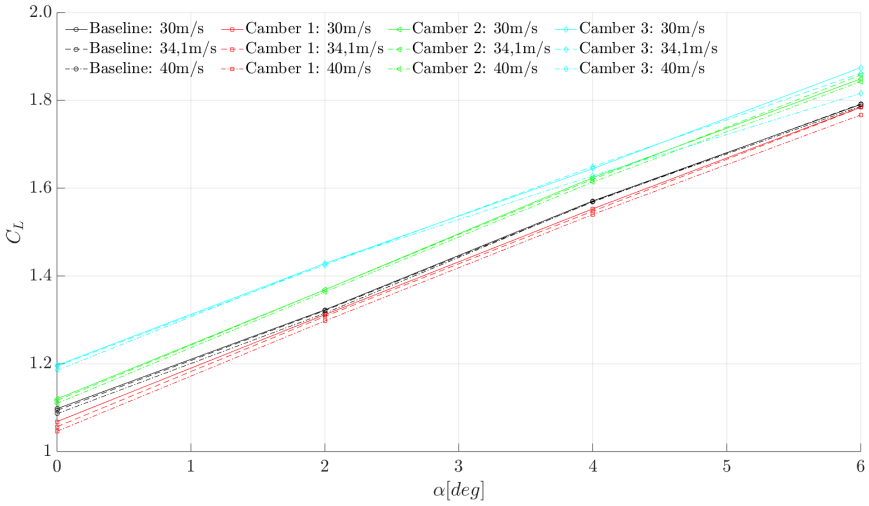

(b) Landing

Figure 14: Lift coefficient (C_L) as function of angle of attack.

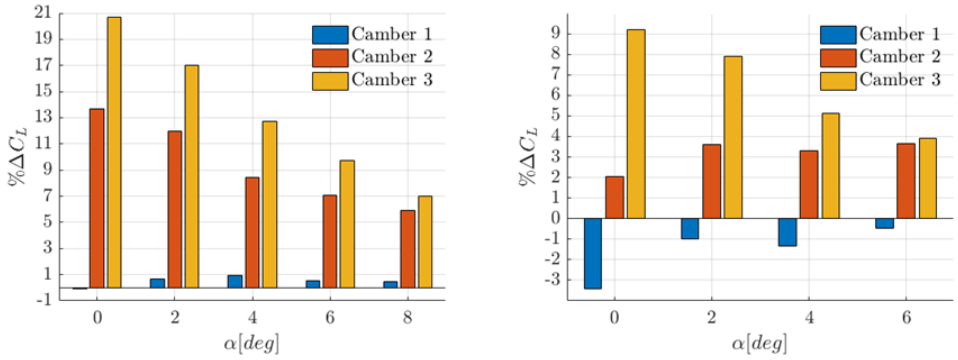

(a) Take-off (b) Landing

Figure 15: Variation of lift coefficient (C_L) with respect to baseline configuration, V_∞ = 34.1 m/s.

A similar behaviour of the $C_L - \alpha$ curves is observed for the landing configuration, as shown in Fig. 14(b). The lift increase provided by the shapes with higher camber is evident also for this configuration, while the effect of the free-stream velocity related to Reynolds number and deformation is still negligible. The quantitative analysis shown by the histogram in Fig. 15(b) highlights that Camber 1 provides a slight decrease of lift, while Camber 3 provides an apparent increase of the C_L even if the percentage variation is lower with respect to the take-off configuration, i.e. from 9% increase at $\alpha = 0°$ to 4% at $\alpha = 8°$.

Figure 16 shows the pressure-drag coefficient C_D as a function of the angle of attack for both the take-off and the landing configuration at the three free-stream velocities investigated in this campaign. Of course the pressure drag does not correspond to the whole aerodynamic drag that includes the friction drag also. Nevertheless, the pressure drag is dominant at high angle of attack [**?**] so that the trend of its variations can be taken as representative of the trend of the total drag variation.

In particular, for the take-off configuration, Fig. 16(a) shows an evident

increase of the pressure drag related to the increase of the morphing-flap camber. Differently from what observed for lift coefficient, the pressure-drag coefficient depends significantly on the wind speed. In particular, a significant decrease of the pressure-drag coefficient can be observed as the wind speed is increased. This behaviour could be explained by the morphing-flap deformation provided by an increasing aerodynamic loading that could produce a local decrease of the angle of attack, and by the increase of the Reynolds number that leads to a thinner boundary layer and could delay separation. These effects provide reduced pressure-drag coefficients for all cambers and angles of attack tested.

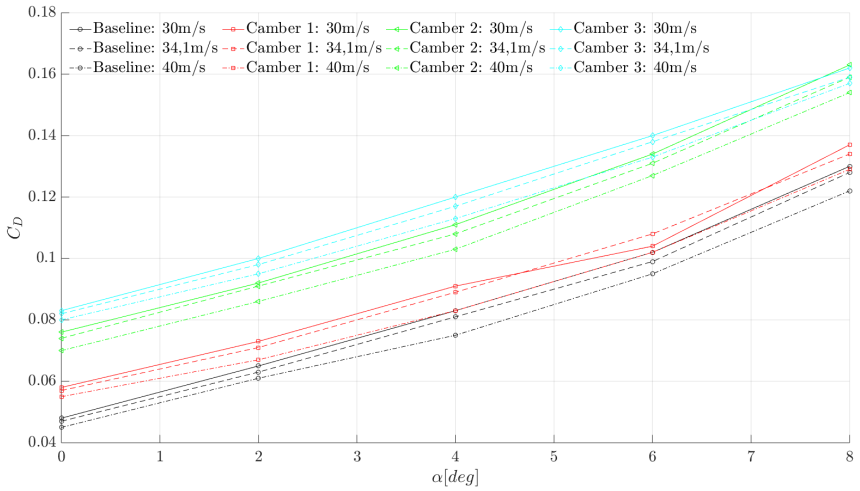

(a) Take-off

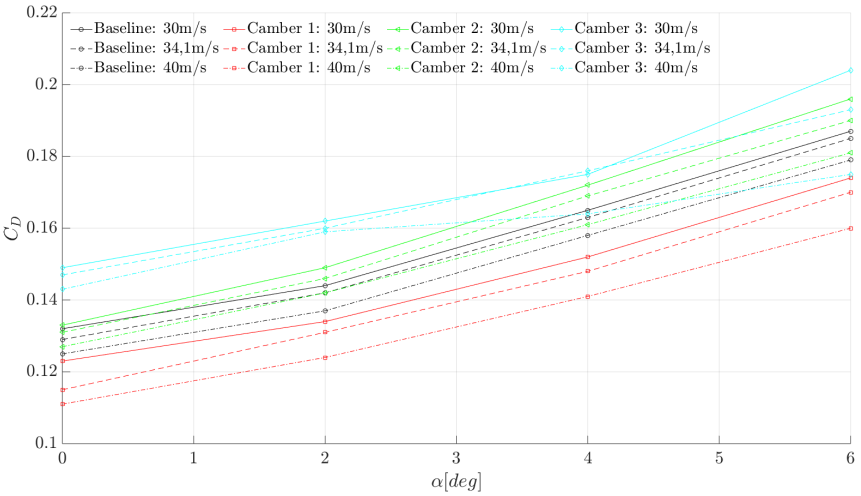

(b) Landing

Figure 16: Pressure-drag coefficient (C_D) as function of the angle of attack.

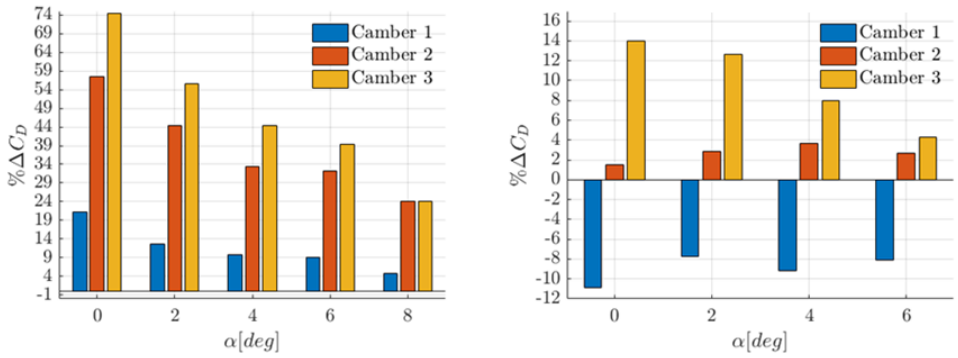

(a) Take-off (b) Landing

Figure 17: Variation of the pressure-drag coefficient (C_D) with respect to the baseline configuration, $V_\infty = 34.1$ m/s.

The quantitative evaluation of the pressure-drag variation with respect to the baseline configuration, shown in Fig. 17(a) for the mid free-stream velocity tested, highlights the monotonic increase of C_D with camber, while a monotonic decrease of the C_D is observed increasing the angle of attack for all the investigated shapes of the morphing flap in take-off configuration.

For the landing configuration, Fig. 16(b) shows that Camber 1 configuration of the morphing flap produces a decrease of the pressure drag of the entire wing. The quantitative evaluation presented in Fig. 17(b) shows that a decrease of about 8% of the pressure drag with respect to baseline configuration can be obtained with Camber 1 for the mid free-stream velocity tested. Camber 2 does not influence the pressure drag contribution of the entire wing significantly, as an increase of about 2% is observed for all the tested angles of attack. On the other hand, Camber 3 provides a remarkable increase of the pressure drag, particularly at the lower angles of attack. The behaviour of the pressure-drag curves with respect to the free-stream velocity indicates that the Reynolds number and model deformation have a stronger impact on drag than on lift, with variations in the order of 10% against 1%.

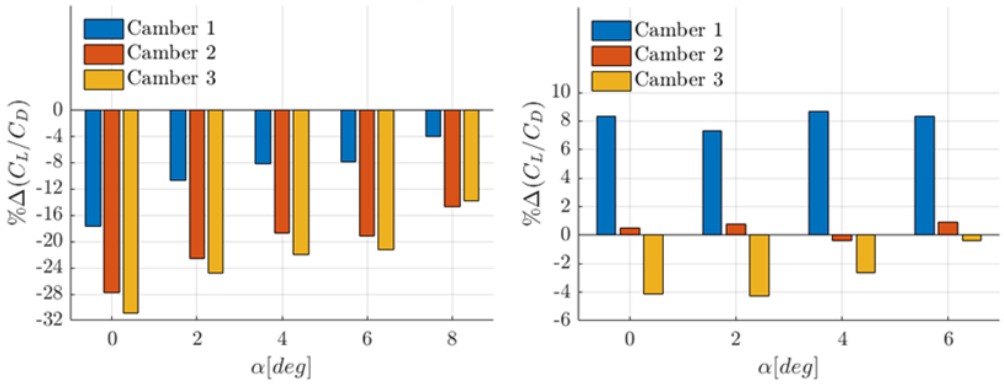

(a) Take-off (b) Landing

Figure 18: Variation of the wing efficiency with respect to the baseline configuration, V_∞ = 34.1 m/s.

Figure 18 shows the variation of the wing lift-to-pressure-drag ratio obtained by morphing the flap with respect to the baseline configuration for the mid free-stream velocity tested. In particular, for the take-off configuration, Fig. 18(a) shows that all the cambered morphing configurations provide a reduction of the wing efficiency. This benefit is reduced as the angle of attack increases. On the other hand, for the landing configuration, Fig. 18(b) shows that Camber 1 configuration provides a remarkable increase of the wing lift to pressure drag in the order of 8% with respect to the baseline configuration. Camber 2 does not provide an appreciable variation of this quantity in landing configuration, while Camber 3 slightly decreases the wing efficiency with respect to baseline configuration.

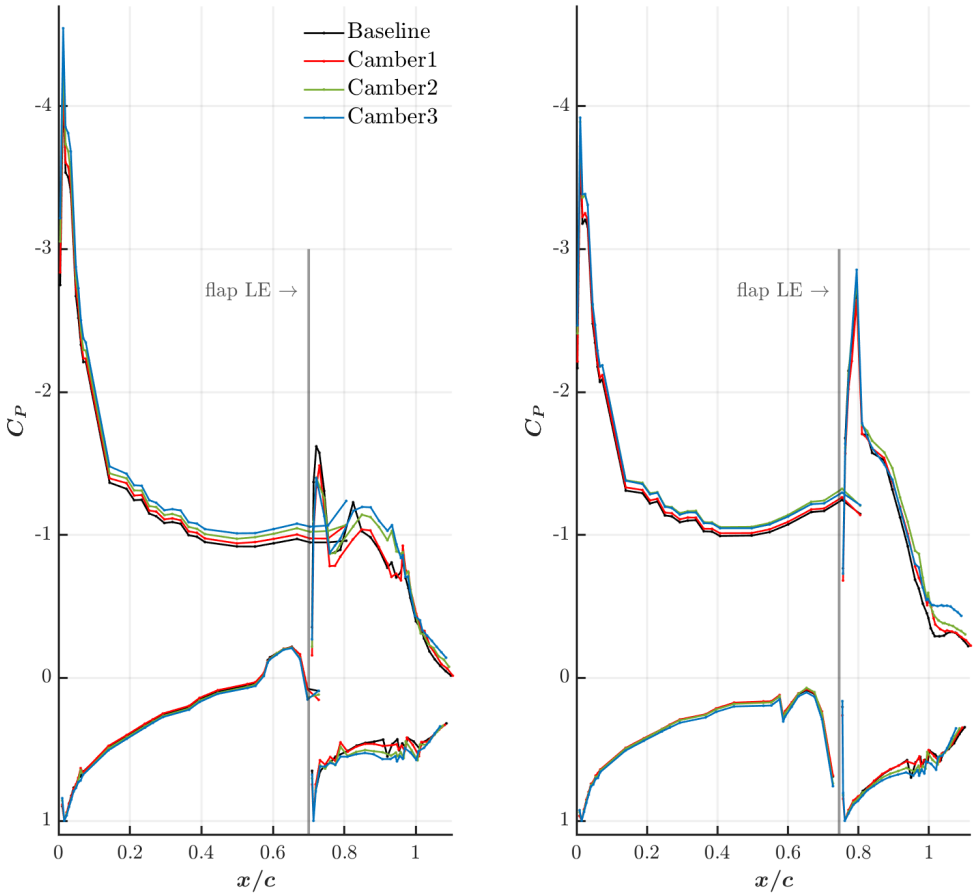

(a) Take-off - $\alpha = 8°$ (b) Landing - $\alpha = 6°$

Figure 19: Distribution of the pressure coefficient on the symmetry plane, $V_\infty = 34.1$ m/s

Further insight into the behaviour of the flow over the wing is provided by the comparison of the pressure-coefficient C_P distribution measured on the symmetry plane for the different morphing-flap configurations. Figure 19 shows the C_P distributions measured at the highest angles of attack tested for the take-off and landing configuration for a free-stream velocity $V_\infty = 34.1$ m/s.

The C_P distributions measured in take-off configuration (see Fig. 19(a)) show that the increased flap camber is responsible for an increase of the suction peak on the upper surface in the leading-edge region of the main wing. In general, this effect is combined with a higher suction on the whole upper surface of the main-wing airfoil. On the other hand, the pressure distribution measured on the flap shows that the local suction peak at the leading edge decreases with increasing camber. In contrast, the effect of camber provides an increase of the suction particularly evident in the central region of the flap upper surface. Consequently, a higher aerodynamic loading is applied to the morphing flap with increasing camber that could be responsible of the deformation of the flap airfoil section; this fact is similar to the one discussed earlier considering the effects of the increasing free-stream velocity on the aerodynamic coefficients measured. Moreover, the pressure-coefficient behaviour is very similar for all geometries in the aft portion of the flap, except for Camber 3 that shows a slightly higher suction in this region at this angle of attack.

In landing configuration, the pressure measurements of the C_P distributions on the suction side of the main wing show a behaviour similar to the take-off configuration, see Fig. 19(b). Indeed, the increased camber, due to the different morphing-flap configurations, provides an increase of the suction on the upper surface and, particularly, an increase of the suction peak on the leading edge of the main wing. Differently from what observed for the take-off configuration, in landing the pressure distributions measured on the flap show that the local suction peak at leading edge is lower for the flap configurations characterised by increasing camber. Moreover, the quite flat distributions of C_P observed at trailing edge region of the flap for all the geometries highlight a separated flow in this area, as confirmed by PIV

measurements reported later on. In particular, the Camber 3 configuration of the flap provides an increase of suction at the trailing region particularly evident with respect to the baseline configuration.

3.2. Flow-field measurements

The PIV surveys performed over the suction side of the morphing flap were suitable to investigate in more detail the flow physics involved in the flap functioning for some selected test cases. In particular, Fig. 20 shows the comparison of the in-plane velocity magnitude measured for the take-off configuration at $V_\infty = 34.1$ m/s with the baseline and Camber 1 flap shapes at different angles of attack, i.e. $\alpha = 4°, 6°, 8°$.

In all the flow field representations, it is possible to notice the presence, the position and the intensity of the wake of the main wing in the region of investigation, in particular in the upper left part of the measurement windows. This wake is well separated from the boundary layer of the flap, so that the interaction of the two rotational regions is negligible. The comparison between the flow measurements performed with the baseline flap configuration (see Fig. 20(a)) and Camber 1 configuration (see Fig. 20(b)) shows that the cambered shape produces an incipient flow separation near the trailing edge. This is highlighted by the higher distance, with respect to the baseline configuration, separating the streamlines in this area and by the low speed region, coloured in blue, near the airfoil surface. This separation region produces a thickening of the boundary layer near the trailing edge, thus increasing the pressure drag.

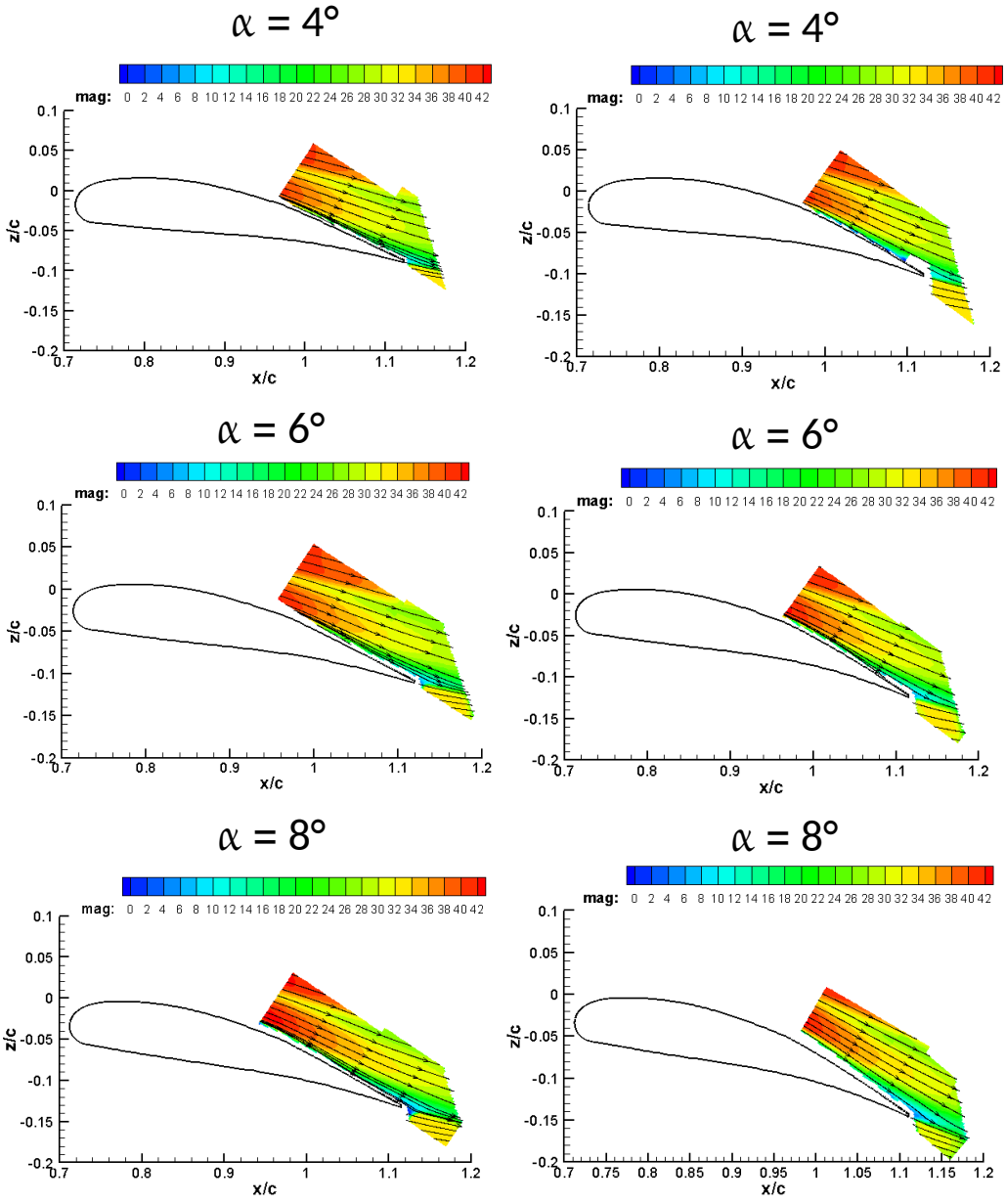

(a) Baseline (b) Camber 1

Figure 20: Average in-plane velocity magnitude measured by PIV in the symmetry plane of the morphing flap for the take-off configuration, $V_\infty = 34.1$ m/s.

PIV results for the landing configuration are reported in Fig. 21 showing the comparison of the in-plane velocity magnitude measured at $V_\infty = 34.1$

m/s with baseline, Camber 1 and Camber 2 flap shapes at two different angles of attack, i.e. $\alpha = 0°, 2°$.

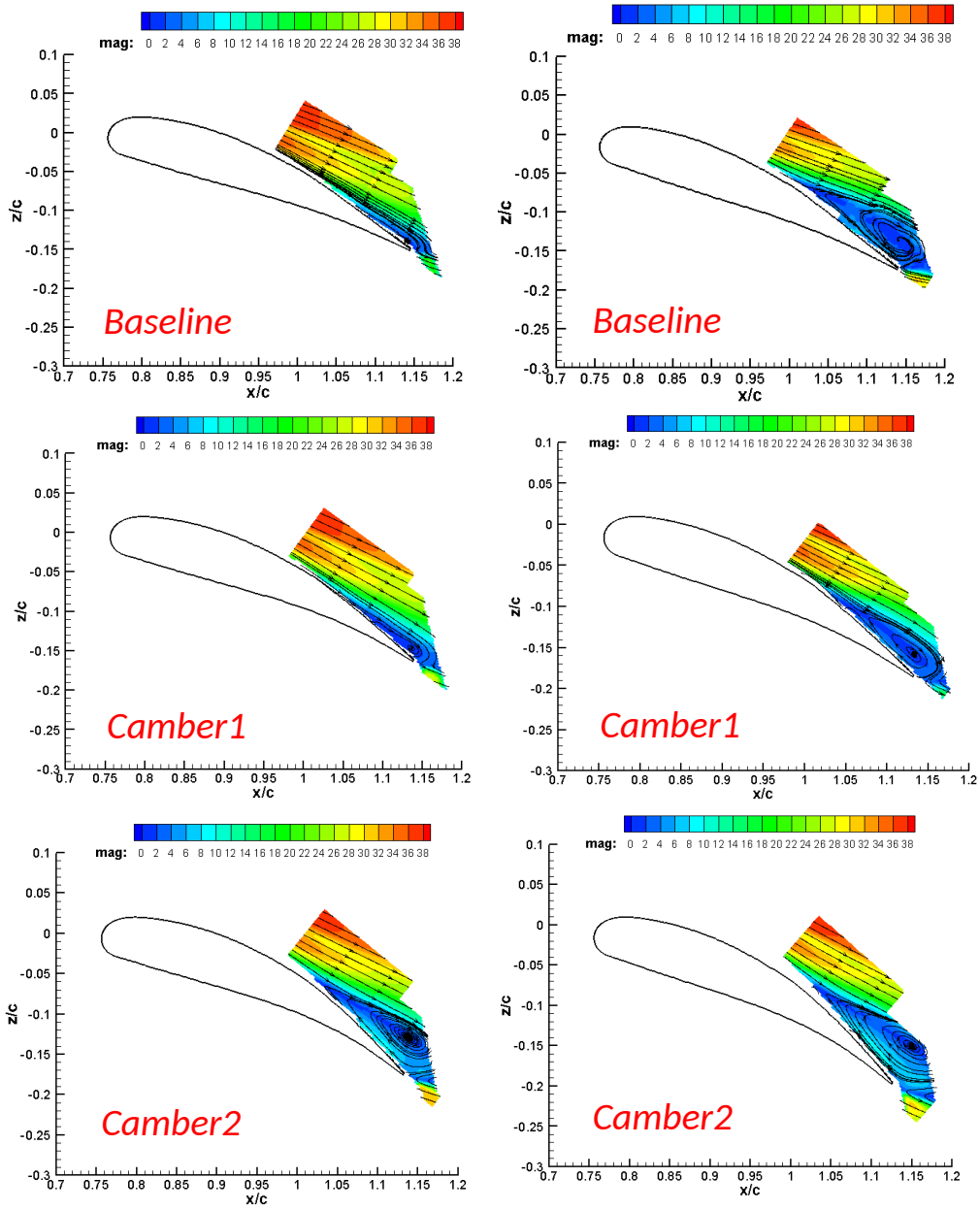

(a) $\alpha = 0°$ (b) $\alpha = 2°$

Figure 21: Average in-plane velocity magnitude measured by PIV on the symmetry plane of the morphing flap for the landing configuration, $V_\infty = 30$ m/s.

Unlike in the take-off case, for the landing configuration the flow fields show large separated regions in the trailing-edge area of the flap for the highest angles of attack. This feature was already discussed when analysing the distribution of the C_P that shows an almost flat behaviour in a rather large portion of the flap surface near the trailing edge.

A quite different behaviour of the flow fields is observed for different flap cambers. For $\alpha = 0°$, a low-speed region can be observed at the trailing edge of the baseline flap indicating an incipient separation of the flow. For Camber 1, the area of the separated flow is quite similar, while increasing the camber of the morphing flap (Camber 2) a quite extended flow separation, characterised by a large separation bubble, is present. Increasing the angle of attack to $\alpha = 2°$, the area of the separated flow region is increased for all the flap configurations. However, Camber 1 is the flap shape that produces a reduction of the large separation bubble observed in the baseline configuration, thus confirming the benefit observed from the airfoil performance evaluation. On the other hand, the flap configuration with increased camber provides an increase of the size of separated flow region at the trailing edge with respect to the baseline configuration, thus confirming that Camber 2 does not produce a benefit in terms of drag.

3.3. Shape measurements

The main goal of the shape measurements was to evaluate the deformation of the morphing flap under aerodynamic load with respect to the reference case without wind. In particular, these tests were performed with a maximum free-stream velocity of 30 m/s for safety reasons related to the use of the complex optical set-up. Figure 22 shows the displacements of the suction side of the morphing flap along the three axes of the reference system, described in Sec. 2.3.3, for the take-off test configuration at $\alpha = 8°$ with Camber 3.

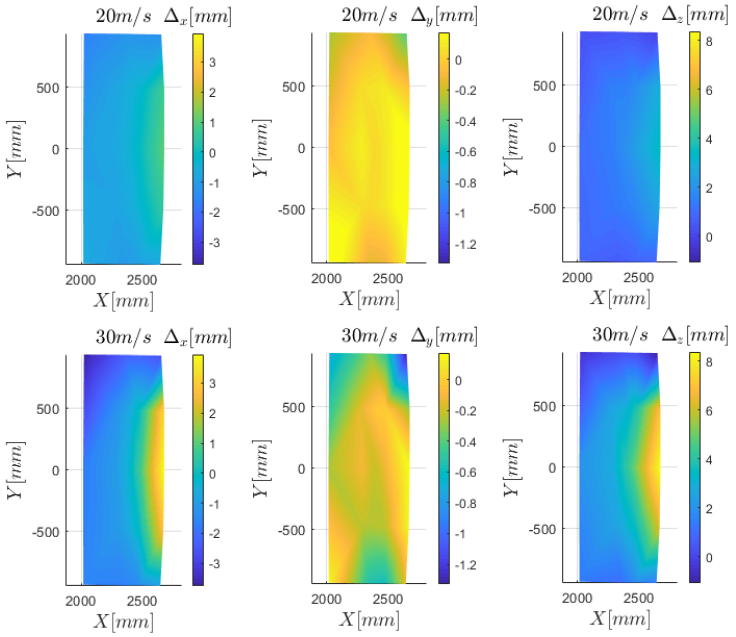

Figure 22: Displacement of the suction side of the morphing flap for the take-off configuration, Camber 3, $V_\infty = 30$ m/s, $\alpha = 8°$.

The shape measurements confirm a good symmetry of the displacement, and therefore of the flow. In particular, the displacements along the spanwise direction (Y) are lower with respect to those in the longitudinal (X) and vertical (Z) directions, as expected. Owing to the applied constraints, the distribution of the displacement along the X and Z directions shows that the deformation mainly concerns the trailing edge of the flap, in the central region. In particular, the highest displacement measured for $V_\infty = 30$ m/s is below 1% of the flap chord.

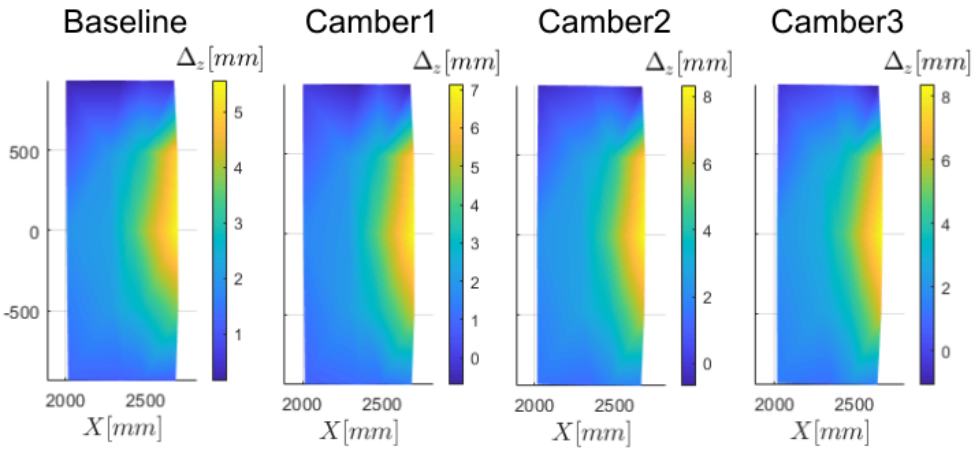

Figure 23: Effect of the camber on the vertical displacement of the suction side of the morphing flap for the take-off configuration, $V_\infty = 30$ m/s, $\alpha = 8°$.

Moreover, increasing the camber of the morphing flap, greater vertical deformations are observed as presented in Fig. 23 showing the vertical displacements measured for different cambers in the same test condition of Fig. 22.

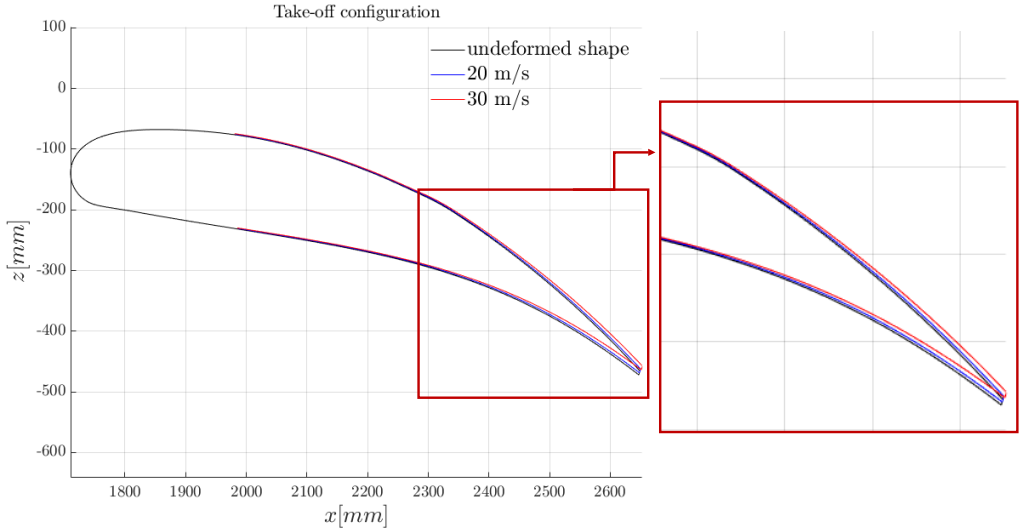

(a) Take-off

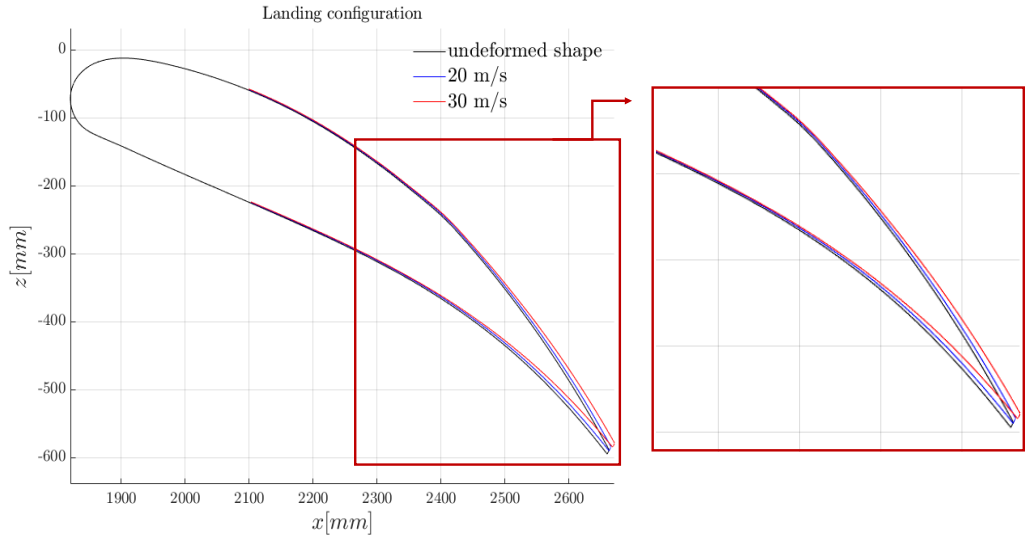

(b) Landing

Figure 24: Comparison of the deformed airfoil shapes of the flap for Camber 3 configuration, $\alpha = 8°$.

In order to obtain the displacement of the complete airfoil section of the flap, the results found for the suction side were extended to the pressure

side under the hypothesis that the thickness of the flap does not change significantly under the aerodynamic load. Figure 24 shows the comparison of the deformed flaps with respect to the Camber 3 reference geometry as a function of the velocity for both take-off and landing configurations.

The airfoil shape comparison highlights that deformations are not negligible, particularly in the trailing edge region of the morphing flap, thus confirming the effect of the flap deformation on the aerodynamic loads.

4. CONCLUSIONS

A comprehensive experimental campaign was performed in the large wind tunnel of Politecnico di Milano to characterise the performance of a wing section equipped with a high-lift morphing device, a flap. An almost full-scale prototype of the main wing of a large passenger aircraft equipped with the flap was used for the tests. The design of the wind tunnel tests was detailed, as part of the scope of this work was to investigate and disseminate the set-up to perform a complex experimental activity involving the use of wing models with dimensions near to full scale.

Several measurement techniques were used in the test campaign. Pressure measurements performed on the mid-span section of the wing model allowed the evaluation of the aerodynamic effects for different morphed shapes provided by the flap in take-off and landing flight conditions. The measurements showed a remarkable increase of the lift due to flap increased camber, particularly an increase of at least 7% and 4% with respect to the baseline configuration for take-off and landing conditions, respectively, at the highest angle of attack tested. Moreover, the lowest cambered shape of the morphing flap tested provides a decrease of the pressure drag contribution in the landing configuration, leading to an increase of the aerodynamic efficiency

of the wing of about 8% with respect to the baseline configuration. On the other hand, the increase of pressure drag contribution found for all the cambered shapes of the flap in take-off condition does not provide a benefit on the wing performance in terms of aerodynamic efficiency with respect to baseline configuration.

PIV measurements enabled the investigation of the flow physics involved in the aerodynamic performance of the morphing flap. In particular, the survey of the flow field over the suction side of the flap showed an attached boundary layer in the take-off configuration for almost all the cambered shapes, with the presence of a thin region of incipient flow separation at the trailing edge occurring with high camber of the flap. On the other hand, the flow field in landing conditions showed a large region of flow separation at the trailing edge that is significantly reduced for the morphing flap shape characterised by the lowest camber, thus confirming the benefits observed from the evaluation of the aerodynamic performance.

An optical non-intrusive shape measurement was used to check the deformation of the airfoil sections of the flap under aerodynamic loading. The measurements showed that the highest deformations of the flap are present in the trailing edge, particularly in the central region. The vertical displacements observed at the flap trailing edge were in the order of a few percents of the flap chord, thus confirming that the deformation of the flap shape provides a non-negligible effect on the aerodynamic performance of the wing, as shown by the load measurements at different free-stream velocities.

In conclusion, it can be said that the present activity demonstrated that the performance of a flapped wing can be improved by means of relatively small flap morphing although, for the specific tested shapes, only in landing case the variations were beneficial (with a consistent increase of lift coeffi-

cient). This result, for example, indicates that the required maximum lift coefficient can be obtained with lower flap extension, with consequent mechanical benefits. Even if we cannot claim that the optimal shapes of the flap were actually obtained for the take-off and landing configurations, nonetheless the current study shows the potential of morphed flap configurations to increase aerodynamic performance for large-scale fixed-wing aircraft.

Acknowledgements

This project has received funding from the European Union's H2020 program for research, technological development and demonstration under grant agreement no 723402.